

Determining quantum phase diagrams of topological Kitaev-inspired models on NISQ quantum hardware

Xiao Xiao,¹ J. K. Freericks,² and A. F. Kemper^{1,*}

¹*Department of Physics, North Carolina State University, Raleigh, North Carolina 27695, USA*

²*Department of Physics, Georgetown University, 37th and O Sts. NW, Washington, DC 20057 USA*

Topological protection is employed in fault-tolerant error correction and in developing quantum algorithms with topological qubits. But, topological protection *intrinsic to models being simulated*, also robustly protects calculations, even on NISQ hardware. We leverage it by simulating Kitaev-inspired models on IBM quantum computers and accurately determining their phase diagrams. This requires constructing conventional quantum circuits for Majorana braiding to prepare the ground states of Kitaev-inspired models. The entanglement entropy is then measured to calculate the quantum phase boundaries. We show how maintaining particle-hole symmetry when sampling through the Brillouin zone is critical to obtaining high accuracy. This work illustrates how topological protection intrinsic to a quantum model can be employed to perform robust calculations on NISQ hardware, when one measures the appropriate protected quantum properties. It opens the door for further simulation of topological quantum models on quantum hardware available today.

I. INTRODUCTION

Quantum computers are fragile and susceptible to rapid decoherence [1], and the use of topological protection has been proposed as a potential remedy. Typically, there are two propositions to make quantum computation practical for deep circuits: (i) fault-tolerant quantum computers, which use logical qubits and error correcting codes (like the surface code) to correct all errors that appear during computation [2–11] and (ii) topological quantum computers, which use topological qubits, naturally protected from the environment, to perform intrinsically error-free computations [12–14]. Here, we propose a third avenue: when the model under study has non-trivial topological invariants, the model’s topological properties (rather than the hardware’s) can be leveraged to identify its sharp phase transitions as the parameters are tuned.

A paradigmatic example of a ground state with non-trivial topological properties, occurs in the Kitaev spin model on the honeycomb lattice [15], which has spawned a class of related models with similar properties [16–41]. Their solution involves the braiding and fusing of anyons (in this case Majorana fermions), just as algorithms employing topological qubits do. Ideally, topological quantum computers could be used to solve models of this type. Unfortunately, it has proved to be extremely difficult to create topological qubits in quantum hardware [42].

In this work, we illustrate that these Kitaev-inspired models can be solved on conventional quantum computers with the braiding operations encoded in low-depth conventional quantum gates. Moreover, we can utilize the distinct topological properties of ground states to clearly distinguish the phase transitions in this class of models for system sizes where noise makes this difficult. These topological quantum simulations are carried out on

IBM’s transmon-based conventional quantum computing hardware.

Typically, determining the phase boundaries in these models is challenging because they lack a local order parameter. The standard approach is to calculate the entanglement entropy [43, 44], but this requires a large system size, beyond what is currently available in NISQ machines. Instead, we develop and use particle-hole symmetry-enforced circuits encoding twisted boundary conditions, enabling determination of ground-state properties through the entire Brillouin zone with only a modest number of qubits. Due to the discrete topological nature of the quantum phase transition, these circuits can identify the different phases by revealing discontinuities in the entanglement entropy even if the jump at the discontinuity is diminished due to noise.

II. RESULTS

A. Kitaev-inspired models and quantum circuit construction

Kitaev’s model has spins distributed on a honeycomb lattice with nearest-neighbor spin couplings $J^\alpha \sigma_i^\alpha \sigma_j^\alpha$ that depend on the bond direction [15]. In the above, $\alpha = x, y, z$ stands for a certain coordinate component in real space, and i (j) is an index labeling the site in the honeycomb lattice. The model is solved by fermionization; we use Jordan-Wigner strings that are oriented along the x, y bonds (see Fig.1). Many Kitaev-inspired models generalize this geometry to include structures such as chains and 2-leg ladders and generalize the interactions to include non-Ising-like couplings such as $\sigma_i^x \sigma_j^y$. For an exact solution to exist, the lattice geometry and interactions must conform to a broad set of rules [40]. We consider two particular models: the original honeycomb lattice and a one-dimensional variant (called the Kitaev spin chain), which is a chain extracted from the original Kitaev hon-

* akemper@ncsu.edu

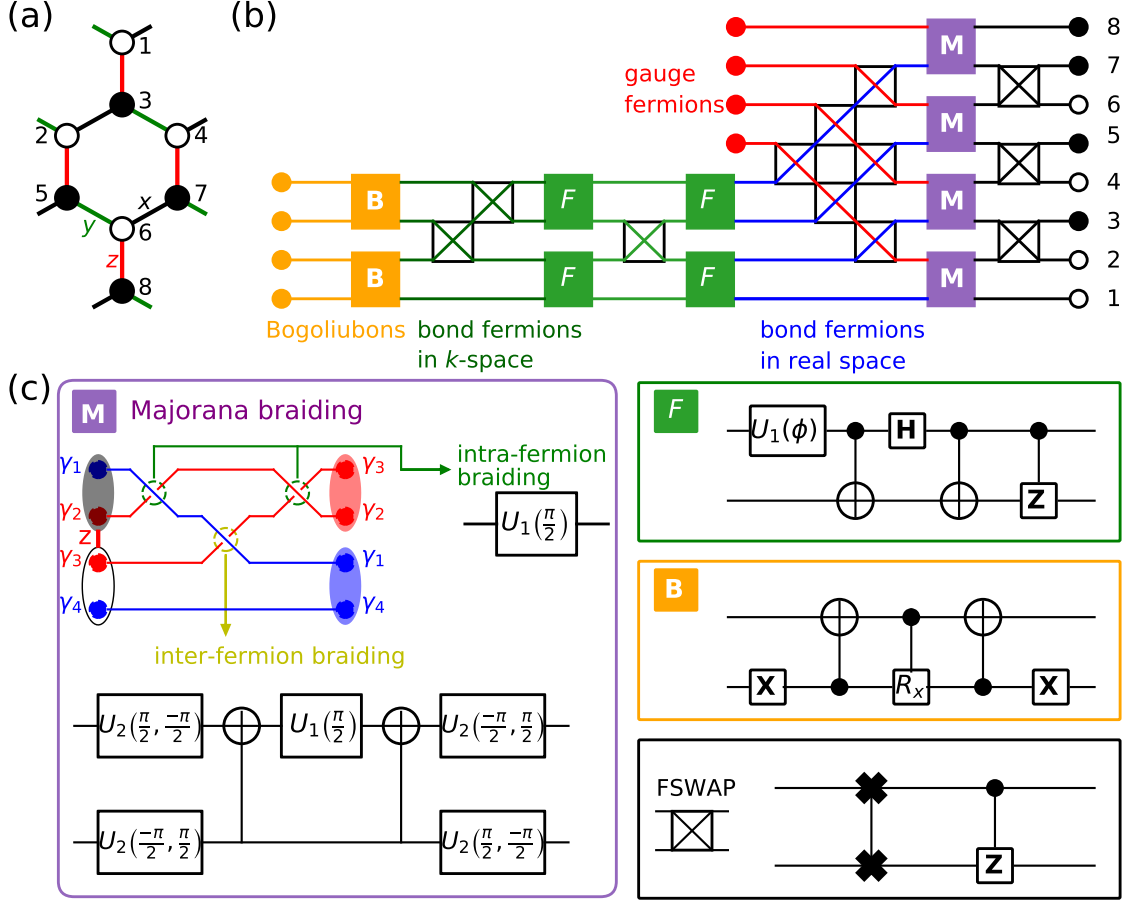


FIG. 1. Quantum circuit for the Kitaev honeycomb model with braiding. (a) The lattice structure of the Kitaev honeycomb model with the numbers denoting the ordering along the Jordan-Wigner string; (b) the quantum circuit used to prepare the ground-state wave function (each qubit is initially at the $|0\rangle$ state); (c) detail of the elements of the quantum circuit shown in (b). In (a) the x -, y - and z -bonds are shown in black, green and red respectively. The operation F shown in (c) stands for Fourier transformation operations in (b), the operation B in (c) denotes Bogoliubov transformation operations in (b), and the FSWAP operation in (c) stands for the operation exchanging the order of the neighbored qubits representing fermions in (b). The U_1 and U_2 operations in (c) are special cases of the general single-qubit operation $U_3(\theta, \phi, \lambda)$ specified by three angles θ , ϕ , and λ [45]. Explicitly, $U_1(\lambda) = U_3(0, 0, \lambda)$ and $U_2(\phi, \lambda) = U_3(\pi/2, \phi, \lambda)$.

eycomb model by turning off the J^y couplings.

After the Jordan-Wigner transformation, z - z spin couplings map to fermion-fermion interactions, making the effective fermion model interacting. But in Kitaev-inspired models, these terms can be simplified by Majorana braiding: the fermions at each site are split into two Majorana fermions, braided both internally and with a neighbor connected by a z -bond (see Appendix A and C for details) and then recombined into two new fermions. The first is an itinerant bond-centered fermion (on the z -bonds) and the second is a set of conserved gauge fermions (one per z -bond).

Thus, the original spin model is fermionized into bond fermions and gauge fermions that act as local chemical potentials. As long as we are interested in the ground state, the gauge fermions do not play any further role [15, 43]. The eigenstates in the free fermion sector are

found by Fourier transformation followed by Bogoliubov transformation [46, 47]. A schematic of the quantum circuit that performs these steps is given in Fig. 1(b) and (c).

The braiding circuit in Fig. 1(c) accounts for the non-trivial phase changes due to the braiding of two Majorana fermions [48, 49]:

$$B_{i,j}^{\pm} = \frac{1}{\sqrt{2}} (1 \pm \gamma_i \gamma_j), \quad (1)$$

where \pm denotes the clockwise and counterclockwise braidings of the two Majorana fermions γ_i and γ_j . There are two different types of braidings, intrafermion and interfermion.

The intrafermion braiding operator relates to the

Jordan-Wigner fermions via

$$B_{in} = \frac{1}{\sqrt{2}} [1 \pm i (c^\dagger c - c c^\dagger)], \quad (2)$$

which is a single-particle operation [see Fig. 1(c)] and can be realized by a phase gate in quantum circuits. The interferion braiding is more complex, and can be expressed as (see Appendix A for details):

$$B_{ex} = \frac{1}{\sqrt{2}} [1 \pm i (c_1^\dagger c_2^\dagger - c_1^\dagger c_2 + c_1 c_2^\dagger - c_1 c_2)]. \quad (3)$$

From the matrix representation of B_{ex} , we construct a quantum circuit realizing the braiding by two CNOT gates in combination with single-qubit gates [50] (Fig. 1(c)). In these operations, we must abide by the local constraints imposed by the Hamiltonian (see Appendix C for details).

With the braiding circuit in hand, we apply them to the 8-site Kitaev honeycomb lattice and the 4-site Kitaev spin chain and obtain the entanglement entropy for a subsystem (A) by measuring the density matrix with the help of the maximum likelihood estimator [51]. While this approach clearly does not scale, it is feasible for these size systems. Fig. 2 shows the entanglement entropy for the subsystem A illustrated in green in Figs. 2(a) and (b) as we vary one of the exchange constants. The results from the quantum circuit simulator and the exact results agree up to statistical noise (see Appendix D for the ground-state energies). The results from the quantum hardware, although they show similar trends, exhibit significant deviations from the exact results due to

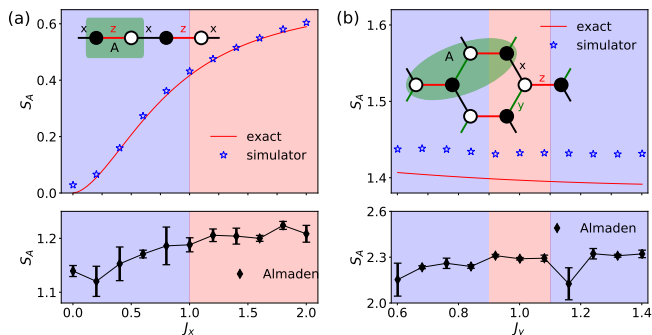


FIG. 2. Quantum simulation of the entanglement entropy of Kitaev-inspired models: (a) the 1D Kitaev spin chain with $J_z = 1$ and varying J_x ; (b) the 2D Kitaev spin model on the honeycomb lattice with $J_z = 1$, $J_x = 0.1$ and varying J_y . In both (a) and (b), the lattice structure and the definition of the subsystem ‘ A ’ (the green shaded parts) are shown in the insets of the upper panels, the comparison of the exact results and the results from the simulator are shown in the upper panel, and the results from IBMQ-Almaden are shown in the lower panel. Each data point from IBMQ-Almaden were obtained by performing 5 independent experiments, and for each of them $N = 8196$ shots were used. The simulator data for the 1D Kitaev spin chain was obtained by $N = 8196$ shots, while the simulator data for the 2D Kitaev spin model was obtained by $N = 81960$ shots.

machine errors. Nevertheless, the circuits do correctly capture the braiding operation that is fundamental to the solution of the Kitaev-inspired models and to the simulation of a topological quantum computer.

B. Symmetry-enforced quantum circuits

The ranges of exchange parameters in Fig. 2 cover a regime where both models have quantum phase transitions (in the thermodynamic limit). We observe no signature of these transitions due to finite-size effects (see Appendix E for details); however this limitation of NISQ machines can be overcome for the Kitaev-inspired models by employing a grid of shifted momenta.

The Kitaev-inspired models reduce to a block-diagonal form in momentum space after they have been converted to the Majorana-Fermion representation. But, because a Bogoliubov transformation is still needed to fully diagonalize the problem, one must be careful to preserve particle-hole (PH) symmetry when constructing the quantum circuit. Consider a system containing N unit cells. The discrete Fourier transformation to an arbitrary set of N momentum points in the BZ, $\mathcal{K} = \{2\pi n/N \mid n \in [0, N)\} + \delta k$ can be written as:

$$c_{n,\mathcal{K}} = \frac{1}{\sqrt{N}} \sum_{k \in \mathcal{K}} e^{ikn} c_k, \quad (4)$$

where $c_{n,\mathcal{K}}$ denotes real-space operators obtained by Fourier transformation of the set \mathcal{K} . Here, δk is introduced to shift the momentum points. In the Fourier transformation circuits, the phase shift requires a phase correction [52]. PH symmetry requires that the information from the set must also be included. Hence, the symmetry-enforced Fourier transformation is given by:

$$c_n = \frac{1}{\sqrt{2}} (c_{n,\mathcal{K}} + c_{n,-\mathcal{K}}), \quad (5)$$

which requires a more complex circuit with twice the number of qubits. The demonstration of the symmetry-enforced processes under the particle-hole symmetry for the $N = 2$ case is shown schematically in Fig. 3(a). We maintain two copies of each bond fermion f_i (blue), one for each set $\pm\mathcal{K}$, which are shifted by the corresponding $\pm\delta k$. The corresponding quantum circuit is shown in Fig. 3(b). Since the Bogoliubov transformation mixes $\pm\mathcal{K}$, the correct momentum set is swapped before the transformation, and swapped back after.

By using this circuit, we can obtain the entanglement spectra of the 2-site Kitaev spin chain as we sweep across the Brillouin zone by measuring a fermionic correlation function [53, 54] (see Appendix E for details). When $J_x < J_z$, the entanglement spectra is always gapped [see Fig. 3(c)], while when $J_x > J_z$, the entanglement spectrum is gapless; the gap closes at $\delta k = \pi$ [see Fig. 3(d)].

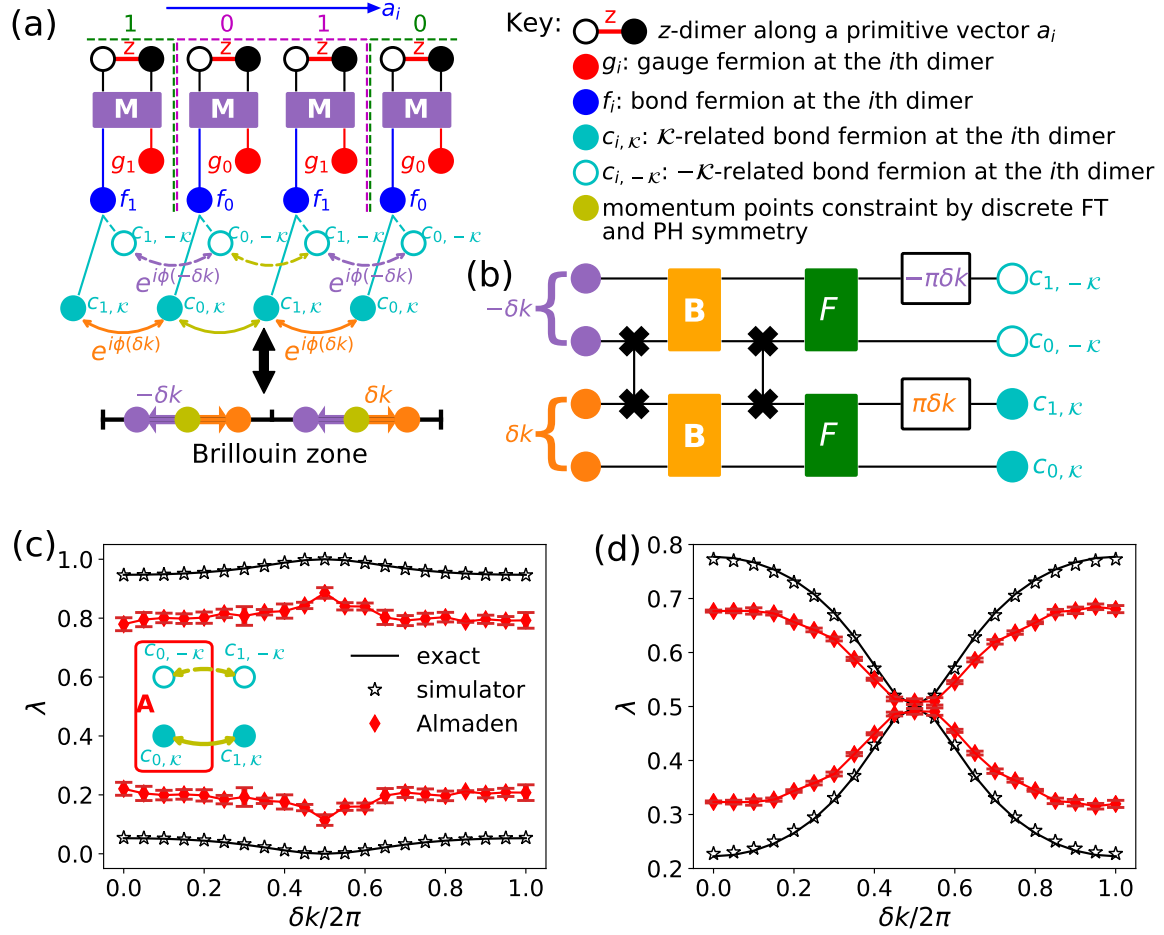


FIG. 3. The symmetry-enforced methodology: (a) symmetry-enforced particle-hole processes in real and momentum space; (b) the symmetry-enforced circuit; (c) the entanglement spectrum of the gapped phase for the 1D Kitaev spin chain with $J_x = 0.5 < J_z = 1$; and (d) the entanglement spectrum of the gapless phase for the 1D Kitaev spin chain with $J_x = 1.5 > J_z = 1$. In (c) and (d), each data point from simulator shown was obtained by $N = 8196$ shots, and each data point from IBMQ-Almaden was obtained from 3 independent experiments, for each of which $N = 8196$ shots were used.

C. Determine phase diagrams of Kitaev-inspired models

The high symmetry points with $\delta k = \pi$ in the BZ are the PH symmetric points, and we expect the quantum phase transition to be dominated by the behavior near these points. Hence, we must ensure the simulation includes the effects of these high-symmetry points, in order to efficiently determine the phase diagram, which we do by the symmetry-enforced quantum circuits discussed above. Using these specific momenta for the larger systems discussed in Fig. 2, we obtain the entanglement entropy (from the same correlation function as above) as a function of exchange parameter, shown in Fig. 4. Although the bond fermion entanglement entropy does not fully capture the system entanglement entropy, the portion that comes from the gauge fermions is featureless [43], and thus sharp transitions may be found by studying the bond fermions alone.

The bond-fermion entanglement entropy for the Kitaev spin chain and honeycomb models are shown in panels (a) and (c). The quantum phase transition is identified by the discrete jump in the entanglement entropy. Using the phase-shifted momenta and the correlation function measurement, the results from the quantum computer now clearly show the phase boundary, even if the magnitude of the jump is reduced. Using this step as the identifying feature, we are able to reconstruct the phase diagram of the two models as a function of both exchange parameters on the IBM-Almaden quantum computer, as shown in Fig. 4(c) and (d). This efficient identification of the phase boundary relies on the difference of the topology of the single-particle wavefunctions in the two different phases. When $|J_i| < |J_j + J_k|$ (with $i, j, k \in \{x, y, z\}$), the single-particle spectrum is gapped, and the ground state of the phase is known as the gapped Z_2 spin liquid in the sense that it can be mapped to the toric code model [15]. On the other hand, when $|J_i| \geq |J_j + J_k|$, the

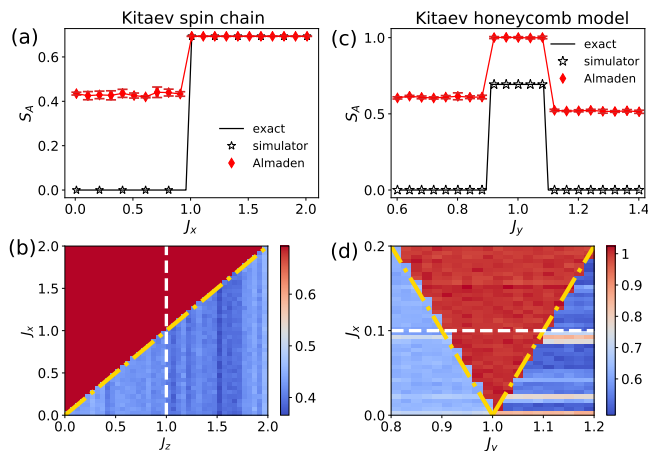


FIG. 4. Quantum phase transitions in Kitaev-inspired models determined by entanglement entropy at high symmetry points: (a/c) The entanglement entropy of bond fermions in the subsystem ‘A’ defined in Fig. 2 for the Kitaev spin chain/honeycomb model by measuring the contribution from high-symmetry points. In (a) we set $J_z = 1$ and vary J_x to probe different phases, while in (c) we probe different phases by tuning J_y and at the same time setting $J_z = 1$ and $J_x = 0.1$. In (a) and (c), each data point from simulator was obtained by using $N = 8196$ shots, while that from IBMQ-Almaden is obtained by 3 independent experiments, for each of which $N = 8196$ shots were used. (b/d) phase diagram of Kitaev spin chain/honeycomb model determined by the IBMQ-Almaden machine. The gold dashed line denotes the exact phase boundary. In the calculation of (d), $J_z = 1$ is assumed. Each data point in phase diagrams shown in (b) and (c) was obtained by IBMQ-Almaden with $N = 8196$ shots.

single-particle spectrum is gapless, and the ground state of the phase is a spinon chiral topological superconductor [55]. The difference in the single-particle spectrum corresponds to edge modes: if the system were terminated with a boundary, then the spinon chiral topological superconducting phase would support edge modes, while the gapped Z_2 spin liquid phase would not. The sharp jumps in Fig. 4 are related to the appearance or disappearance of these edge modes in a finite system. This effect is quite robust, even in the presence of noise; it has its origin in the intrinsic topological nature of the quantum system.

III. CONCLUSION

In this work, we illustrate how the topological properties intrinsic to a quantum model being simulated provides topological protection, resulting in robust quantum calculations, even on NISQ hardware. In particular, we demonstrate how to prepare the ground states of these Kitaev-inspired through low-depth braiding circuits of anyons. By using a particle-hole symmetry-preserving methodology that includes high-symmetry points in the Brillouin zone, the simulation identifies the quantum

phase diagram of both the Kitaev spin-chain and the original Kitaev honeycomb model for systems larger than are otherwise possible on NISQ hardware (when only local quantities are measured). These results directly show how topological protection results in much more robust calculations on NISQ hardware when preparing and determining different quantum phases. The quantum phase diagram was determined by finding discontinuities in the entanglement entropy, which are reduced in magnitude, but still remained easy to identify in this noisy environment. Hence, the benefits of topological-inspired quantum computation can already be realized on NISQ-era conventional quantum computers and this provides a third methodology for topological quantum computation that explores a different realm than quantum error correction or topological quantum computing with topological qubits.

ACKNOWLEDGEMENTS

This work was supported by the Department of Energy, Office of Basic Energy Sciences, Division of Materials Sciences and Engineering under Grant No. DE-SC0019469. J.K.F. was also supported by the McDevitt bequest at Georgetown. We acknowledge use of the IBM Q for this work. The views expressed are those of the authors and do not reflect the official policy or position of IBM or the IBM Q team. Access to the IBM Q Network was obtained through the IBM Q Hub at NC State. We acknowledge the use of the QISKIT software package [45] for performing the quantum simulations. The authors also thank Sonika Johri for insightful comments and Akhil Francis for some technical expertise.

Appendix A: Construction of braiding circuits

When the positions of Majorana fermions change, they braid, and must be described by a braiding circuit. The simplest braiding is the braiding of two Majorana fermions to construct a conventional fermion. A conventional fermion, which can be written as $f = (\gamma_2 + i\gamma_1)/2$, is connected to another conventional fermion defined by $\tilde{f} = (\gamma_1 + i\gamma_2)/2$ via a braiding operation on the Majorana fermions. Recall that the braiding operator (in terms of Majorana fermions) is given by

$$B_{i,j}^{\pm} = \frac{1}{\sqrt{2}} (1 \pm \gamma_i \gamma_j). \quad (\text{A1})$$

In this first example, the two Majorana fermions relate to the same conventional fermion. After expressing the Majorana fermions in terms of the conventional fermions,

we find that

$$\begin{aligned} B_{1,2}^{\pm} &= \frac{1}{\sqrt{2}} [1 \pm i(f^{\dagger} - f)(f + f^{\dagger})] \\ &= \frac{1}{\sqrt{2}} [1 \pm i(f^{\dagger}f - ff^{\dagger})], \end{aligned} \quad (\text{A2})$$

where ff and $f^{\dagger}f^{\dagger}$ vanish due to the Pauli principle. To express this operator as a matrix in the qubit representation, we map the computational basis ($|0\rangle, |1\rangle$) onto the conventional fermion number basis yielding

$$B_{1,2}^{\pm} = B_{in}^{\pm} = \frac{1}{\sqrt{2}} \begin{pmatrix} 1 \mp i & 0 \\ 0 & 1 \pm i \end{pmatrix}. \quad (\text{A3})$$

In the second example, we consider the case of the braiding of two Majorana fermions that belong to two different conventional fermions. The conventional fermions are

$$\begin{cases} f_1 = (\gamma_2 + i\gamma_1)/2, \\ f_2 = (\gamma_4 + i\gamma_3)/2, \end{cases} \quad (\text{A4})$$

when expressed in terms of the different Majorana fermions. There are four different ways to braid these Majorana fermions. Because they are noncommuting operators, we have to carefully specify the ordering scheme. We choose the ascending order for the conventional fermions and for the Majorana fermions within the same conventional fermion. With this specification, we find that the different inter-fermion braidings can be expressed as the product of the braidings within the same fermions and one more braiding, denoted $B_{2,3}^{\pm}$. This is the fundamental braiding between two conventional fermions and is denoted B_{ex} . Replacing γ_2 and γ_3 by f_1 and f_2 , we find that

$$\begin{aligned} B_{ex}^{\pm} &= \frac{1}{\sqrt{2}} \left(1 \pm i(f_1 + f_1^{\dagger})(f_2^{\dagger} - f_2) \right), \\ &= \frac{1}{\sqrt{2}} \left(1 \pm i(f_1^{\dagger}f_2^{\dagger} - f_1^{\dagger}f_2 + f_1f_2^{\dagger} - f_1f_2) \right). \end{aligned} \quad (\text{A5})$$

Again, we use a conventional number basis ($|0_{f_1}0_{f_2}\rangle, |1_{f_1}0_{f_2}\rangle, |0_{f_1}1_{f_2}\rangle, |1_{f_1}1_{f_2}\rangle$), yielding the matrix representation for the inter-fermion braiding

$$B_{ex}^{\pm} = \frac{1}{\sqrt{2}} \begin{pmatrix} 1 & 0 & 0 & \pm i \\ 0 & 1 & \mp i & 0 \\ 0 & \mp i & 1 & 0 \\ \pm i & 0 & 0 & 1 \end{pmatrix}. \quad (\text{A6})$$

Next, we decompose this braiding operation in terms of conventional quantum gates. Since the clockwise braiding is the Hermitian conjugate of the anti-clockwise braiding, we focus on the clockwise braiding. We first consider the braiding within the same fermion, and we notice that

$$B_{in}^{+} = \frac{1}{\sqrt{2}} \begin{pmatrix} 1-i & 0 \\ 0 & 1+i \end{pmatrix} = e^{-i\pi/4} \begin{pmatrix} 1 & 0 \\ 0 & i \end{pmatrix}, \quad (\text{A7})$$

so B_{in} can be realized by the phase gate $U_1(\pi/2)$. Similarly, we find:

$$B_{ex}^{+} = e^{-i\frac{\pi}{4}\sigma_y \otimes \sigma_y}. \quad (\text{A8})$$

So, the quantum circuit can be immediately constructed via the general scheme proposed by Vidal *et al.* [50].

Appendix B: The exact solution of the 1D Kitaev spin chain

The Hamiltonian of the 1D Kitaev spin chain is given by

$$H_{1D} = 4J_z \sum_{i=1}^{N/2} \sigma_{2i-1}^z \sigma_{2i}^z + 4J_x \sum_{i=1}^{N/2} \sigma_{2i}^x \sigma_{2i+1}^x, \quad (\text{B1})$$

where the odd sites belong to the \bullet sublattice while the even sites belong to the \circ sublattice (see the configuration in Fig.1 in the main text). The factor of 4 is added for convenience, as we will see below. To solve this model, we first map the spin model into a fermionic model by the Jordan-Wigner transformation:

$$\begin{cases} \sigma_m^{+} \rightarrow \prod_{j<m} \sigma_j^z c_m, \\ \sigma_m^{-} \rightarrow i \prod_{j<m} \sigma_j^z c_m^{\dagger}, \\ \sigma_m^z \rightarrow \frac{1}{2} (1 - 2c_m^{\dagger} c_m), \end{cases} \quad (\text{B2})$$

where we use the standard mapping $|0\rangle = |\uparrow\rangle$ and $|1\rangle = |\downarrow\rangle$. After fermionization, the Hamiltonian becomes

$$\begin{aligned} \tilde{H}_{1D} &= J_z \sum_i^{N/2} (2n_{2i-1} - 1)(2n_{2i} - 1) \\ &+ J_x \sum_{i=1}^{N/2} (c_{2i} - c_{2i}^{\dagger})(c_{2i+1} + c_{2i+1}^{\dagger}), \end{aligned} \quad (\text{B3})$$

which is identical to the fermionic expression of the Kitaev spin model in the limit $J_y = 0$ [15]. To solve this, we must transform the four-fermion term. We introduce the Majorana fermions on each sublattice $\eta_{\circ/\bullet}$ and $\gamma_{\circ/\bullet}$ [18, 49]:

$$\begin{cases} c_{\circ} = (\eta_{\circ} + i\gamma_{\circ})/2, \\ c_{\bullet} = (\gamma_{\bullet} + i\eta_{\bullet})/2. \end{cases} \quad (\text{B4})$$

The Hamiltonian is re-expressed as

$$\tilde{H}_{1D} = -iJ_x \sum_i \gamma_{i,\circ} \gamma_{i+1,\bullet} + iJ_z \sum_i D_i \gamma_{i,\bullet} \gamma_{i,\circ}, \quad (\text{B5})$$

where $D_i = i\eta_{i,\bullet}\eta_{i,\circ}$ [15, 18] is a local gauge flux. Here i labels unit cells, which have two sublattices \bullet and \circ . Since the Majorana fermions do not have well-defined occupation numbers, we construct quantum circuits after mapping the Majorana fermions back to conventional

fermions. We introduce *bond fermions* for the two sites connected by the z -bonds as follows:

$$f_i = \frac{1}{2} (\gamma_{i,\bullet} + i\gamma_{i,o}). \quad (\text{B6})$$

Finally, we re-express the Hamiltonian again and find

$$\tilde{H}_{1D} = J_x \sum_i (f_i^\dagger - f_i) (f_{i+1}^\dagger + f_{i+1}) + J_z \sum_i D_i (2f_i^\dagger f_i - 1). \quad (\text{B7})$$

Because of the translational symmetry, Lieb's theorem indicates that the fluxes D_i must be uniform [15]. Since D_i commutes with the Hamiltonian \tilde{H}_{1D} , it is a constant of motion. Note that $\eta_o^2 = \eta_\bullet^2 = 1$, so $D_i = \pm 1$.

To diagonalize the Hamiltonian, we start with a Fourier transformation

$$f_n = \frac{1}{\sqrt{N}} \sum_k e^{ikn} \tilde{f}_k, \quad (\text{B8})$$

where the Hamiltonian becomes

$$\tilde{H}_{1D} = \sum_k \Psi_k^\dagger \begin{pmatrix} J_z D + J_x \cos k & iJ_x \sin k \\ -iJ_x \sin k & -J_z D - J_x \cos k \end{pmatrix} \Psi_k, \quad (\text{B9})$$

after dropping some irrelevant constants. Here, we introduce the "spinor"

$$\Psi_k = \begin{pmatrix} \tilde{f}_k \\ \tilde{f}_{-k}^\dagger \end{pmatrix}. \quad (\text{B10})$$

This Hamiltonian in the momentum space can be easily diagonalized through a Bogoliubov transformation. Doing so gives us the final diagonal form

$$\tilde{H}_{1D} = \sum_k E_k (b_k^\dagger b_k - b_{-k}^\dagger b_{-k}), \quad (\text{B11})$$

where $E_k = \sqrt{(J_z D + J_x \cos k)^2 + J_x^2 \sin^2 k}$, and b_k (b_k^\dagger) denotes the annihilation (creation) operator for Bogoliubov fermions with momentum k .

Appendix C: Construction of braiding circuits for specific models

We first describe how different braiding operations affect quantum states. The braiding operations are used to change the positions of Majorana fermions, allowing Majorana fermions belonging to two different conventional fermions to recombine into new fermions. This implies that all braiding processes can be constructed with one inter-fermion braiding and a few intra-fermion braidings. The inter-fermion braiding changes the original two-qubit states into a superposition of their particle-hole partners with a $\pm\pi/2$ phase difference. Intra-fermion braidings behave differently depending on whether they

are performed before or after the inter-fermion braiding. If the intra-fermion braiding is performed before the inter-fermion braiding, it introduces a $\pm\pi/4$ phase to the fermion. However, if the intra-fermion braiding is performed after the inter-fermion braiding, it introduces a superposition of the original state (before inter-fermion braiding) and its particle-hole partner (with a $\pm\pi/2$ phase difference). These basic properties of braiding help us construct braiding circuits based on local constraints.

The first constraint imposed on the braiding operations comes from the local z -bonds. For Kitaev-inspired models, the local fermionic Hamiltonian coupling two sites connected by a z -bond is

$$H_z = J_z (2c_1^\dagger c_1 - 1) (2c_2^\dagger c_2 - 1). \quad (\text{C1})$$

The two-qubit states are $|n_1 n_2\rangle$. This Hamiltonian is re-expressed in terms of bond and gauge fermions as

$$\tilde{H}_z = J_z D (2f^\dagger f - 1), \quad (\text{C2})$$

where D is the local gauge flux and f stands for the bond fermion. The two-qubit states here are $|n_f n_g\rangle$ with n_g denoting the occupation of gauge fermion. The two Hamiltonians and their corresponding states are connected by braiding operations, so the matrix elements of the Hamiltonian (before and after transformation) should be consistent. This implies that the states $|n_f n_g\rangle$ are transformed to the states $|n_1 n_2\rangle$ as follows:

$$\begin{cases} |00\rangle_{f,g} \rightarrow \alpha_{00}^{00} |00\rangle_{1,2} + \alpha_{00}^{11} |11\rangle_{1,2}, \\ |11\rangle_{f,g} \rightarrow \alpha_{11}^{00} |00\rangle_{1,2} + \alpha_{11}^{11} |11\rangle_{1,2}, \\ |10\rangle_{f,g} \rightarrow \alpha_{10}^{10} |10\rangle_{1,2} + \alpha_{10}^{01} |01\rangle_{1,2}, \\ |01\rangle_{f,g} \rightarrow \alpha_{01}^{10} |10\rangle_{1,2} + \alpha_{01}^{01} |01\rangle_{1,2}. \end{cases} \quad (\text{C3})$$

A direct calculation yields

$$\begin{aligned} \langle 00 | H_z | 00 \rangle_{1,2} &= \langle 11 | H_z | 11 \rangle_{1,2} \\ &= -\langle 10 | H_z | 10 \rangle_{1,2} = -\langle 01 | H_z | 01 \rangle_{1,2} = J_z \end{aligned} \quad (\text{C4})$$

and

$$\begin{aligned} \langle 00 | H_z | 00 \rangle_{f,g} &= -\langle 11 | H_z | 11 \rangle_{f,g} \\ &= -\langle 10 | H_z | 10 \rangle_{1,2} = \langle 01 | H_z | 01 \rangle_{1,2} = -J_z D. \end{aligned} \quad (\text{C5})$$

This imposes the constraint $D = 1$ for $n_g = 1$ and $D = -1$ for $n_g = 0$.

This local constraint imposed by the z -bond is general for Kitaev-inspired models. But, the local constraints imposed by other bonds depend on the Jordan-Wigner strings, because those strings determine the ordering of bond fermions emerging from different braiding operations. The details of the braiding circuit of the Kitaev spin model is shown explicitly in the main text, so we demonstrate here how to construct the braiding circuit for the 1D Kitaev spin chain.

Example: The braiding circuit of the 1D Kitaev spin chain: the constraint imposed by the x -bond

To make the discussion explicit, we focus on the x -bond connecting sites 2 and 3. The original Hamiltonian connecting across the x -bond is

$$H_x = J_x \left(-c_2 + c_2^\dagger \right) \left(c_3 + c_3^\dagger \right), \quad (\text{C6})$$

and it is re-expressed in terms of bond and gauge fermions as

$$\tilde{H}_x = J_x \left(f_1^\dagger - f_1 \right) \left(f_2^\dagger + f_2 \right), \quad (\text{C7})$$

where the braiding operations on c_1 and c_2 give the bond fermion f_1 and the braiding operations on c_3 and c_4 give the bond fermion f_2 . Hence, the states considered here contain four qubits. Start with the $n_{g_1} = n_{g_2} = 1$ case. The relevant states for \tilde{H}_x are $|n_{f_1} n_{f_2} n_{g_1} n_{g_2}\rangle = |n_{f_1} n_{f_2} 11\rangle_f$. They are transformed under \tilde{H}_x as

$$\begin{aligned} \tilde{H}_x |0011\rangle_f &= J_x |1111\rangle_f, \quad \tilde{H}_x |1111\rangle_f = J_x |0011\rangle_f, \\ \tilde{H}_x |0111\rangle_f &= J_x |1011\rangle_f, \quad \tilde{H}_x |1011\rangle_f = J_x |0111\rangle_f. \end{aligned} \quad (\text{C8})$$

From the general form of braiding provided by Eq. (C3), we determine the corresponding states in terms of $|n_1 n_2 n_3 n_4\rangle_c$ (relevant to H_x) as follows:

$$\begin{aligned} |0011\rangle &\rightarrow (\alpha_{01}^{01})^2 |0101\rangle_c + \alpha_{01}^{10} \alpha_{01}^{01} |1001\rangle_c \\ &\quad + \alpha_{01}^{01} \alpha_{01}^{10} |0110\rangle_c + (\alpha_{01}^{10})^2 |1010\rangle_c, \\ |1111\rangle &\rightarrow -(\alpha_{11}^{00})^2 |0000\rangle_c - \alpha_{11}^{00} \alpha_{11}^{11} |0011\rangle_c \\ &\quad - \alpha_{11}^{11} \alpha_{11}^{00} |1100\rangle_c - (\alpha_{11}^{11})^2 |1111\rangle_c, \\ |0111\rangle &\rightarrow -\alpha_{01}^{01} \alpha_{11}^{00} |0100\rangle_c - \alpha_{01}^{01} \alpha_{11}^{11} |0111\rangle_c \\ &\quad - \alpha_{01}^{10} \alpha_{11}^{00} |1000\rangle_c - \alpha_{01}^{10} \alpha_{11}^{11} |1011\rangle_c, \\ |1011\rangle &\rightarrow \alpha_{11}^{00} \alpha_{01}^{01} |0001\rangle_c + \alpha_{11}^{00} \alpha_{01}^{10} |0010\rangle_c \\ &\quad + \alpha_{11}^{11} \alpha_{01}^{01} |1101\rangle_c + \alpha_{11}^{11} \alpha_{01}^{10} |1110\rangle_c. \end{aligned} \quad (\text{C9})$$

The action of H_x on these states gives

$$\begin{aligned} H_x |0101\rangle_c &= J_x |0011\rangle_c, \quad H_x |1001\rangle_c = J_x |1111\rangle_c, \\ H_x |0110\rangle_c &= J_x |0000\rangle_c, \quad H_x |1010\rangle_c = J_x |1100\rangle_c, \\ H_x |0100\rangle_c &= J_x |0010\rangle_c, \quad H_x |0111\rangle_c = J_x |0001\rangle_c, \\ H_x |1000\rangle_c &= J_x |1110\rangle_c, \quad H_x |1011\rangle_c = J_x |1101\rangle_c. \end{aligned} \quad (\text{C10})$$

Consistency between Eq. (C8) and (C10) requires

$$\begin{aligned} (\alpha_{01}^{01})^2 &= (\alpha_{01}^{10})^2 = -\alpha_{11}^{00} \alpha_{11}^{11}, \quad (\alpha_{11}^{00})^2 = (\alpha_{11}^{11})^2 = -\alpha_{01}^{01} \alpha_{01}^{10}, \\ \alpha_{01}^{01} &= -\alpha_{01}^{10}, \quad \alpha_{11}^{00} = -\alpha_{11}^{11}. \end{aligned} \quad (\text{C11})$$

This yields $\alpha_{01}^{01} = \pm \frac{i}{\sqrt{2}}$, $\alpha_{01}^{10} = \mp \frac{i}{\sqrt{2}}$, $\alpha_{11}^{00} = \pm \frac{i}{\sqrt{2}}$, and $\alpha_{11}^{11} = \mp \frac{i}{\sqrt{2}}$. Since α_{01}^{01} and α_{11}^{11} are imaginary, there are two intra-fermion braidings acting on the same fermion to adjust the global phase by $\pm i$. The inter-fermion braiding introduces a $\pi/2$ phase difference. To increase the

phase difference to π , one of the intra-fermion braidings is performed after the inter-fermion braiding. We still need to determine on which fermion the intra-fermion braiding acts. Eq. (C11) suggests that:

$$\begin{cases} |01\rangle \rightarrow \alpha_{01}^{01} |01\rangle - \alpha_{01}^{10} |10\rangle, \\ |11\rangle \rightarrow \alpha_{11}^{11} |11\rangle - \alpha_{11}^{00} |00\rangle. \end{cases} \quad (\text{C12})$$

But, the phases introduced by the inter-fermion braiding operations are *opposite* to each other for $|01\rangle$ and $|11\rangle$. To keep the form of Eq. (C12) up to a global minus sign, the only choice is that the intra-fermion braiding operation is applied to the first qubit. This is different for the two states.

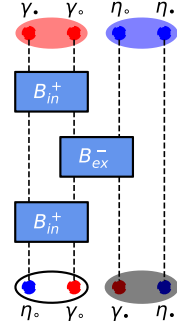


FIG. 5. The braiding circuit used for the 1D Kitaev spin chain.

From the analysis provided above, the braiding circuit must satisfy the following:

1. the circuit is constructed by one inter-fermion braiding and two intra-fermion braidings;
2. one of the intra-fermion braidings is performed after the inter-fermion braiding;
3. the two intra-fermion braiding operations act on the first qubit.

A circuit fulfilling these requirements is shown in Fig. 5. One can apply a similar analysis to the case with $n_g = 0$. One finds the same requirements in that case.

Appendix D: The correctness of the ground state preparation

In this section, we prove that the quantum circuit proposed in the main text (Fig. 1) correctly prepares the ground state of Kitaev-inspired models. The system sizes of the models considered here are the same as those shown in the main text. The lowest energy of the finite-size cluster is determined by exact diagonalization, and then compared to the results obtained by exact solution and quantum circuit simulation. Results for the 1D Kitaev spin chain and the Kitaev spin model are summarized in Fig. 6. It turns out that the lowest energies obtained from exact diagonalization are identical to those obtained from the exact solution. Results

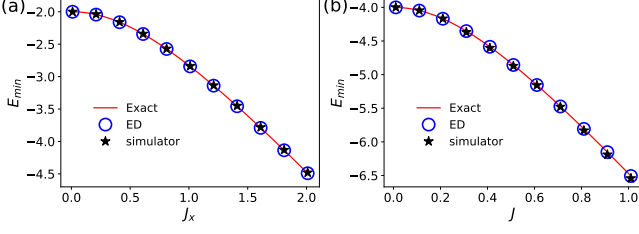


FIG. 6. Verification of the ground-state preparation: (a) the 1D Kitaev spin chain and (b) the Kitaev honeycomb model. For the 1D Kitaev spin chain, we set $J_z = 1$ to determine the lowest energy as a function of J_x . For the Kitaev honeycomb model, we set $J_z = 1$ and $J_x = J_y = J$ to determine the lowest energy as a function of J . Each data point from quantum simulators is obtained by performing $N = 8196$ experiments.

from the quantum simulators have small deviations due to finite-number sampling.

Appendix E: Measuring entanglement entropy by symmetry-enforced circuits

For Kitaev-inspired models, ground states have uniform gauge configurations, which contribute trivially to the entanglement entropy. The non-trivial quantum information is stored in the Brillouin zone of the bond-fermions. We describe here how to extract this information with a quantum circuit.

To begin, the original spin model is mapped to a conventional fermionic model by the Jordan-Wigner transformation followed by a Majorana braiding. In general, the fermionic Hamiltonian can be written as

$$H_f = \sum_{i,j} A_{i,j} f_i^\dagger f_j + \sum_{i,j} B_{i,j} (f_i^\dagger f_j^\dagger + h.c.), \quad (E1)$$

where $A_{i,j}$ is the hopping matrix and $B_{i,j}$ is the pairing matrix. The explicit form of the two matrices depends on the details of models. The entanglement entropy of this Hamiltonian is easily obtained by introducing Majorana fermions $f_i = \gamma_{2i-1} + i\gamma_{2i}$ for each physical fermion. In terms of the Majorana fermions, the entanglement entropy of subsystem A is calculated from the eigenvalues of the correlation matrix \mathcal{C} [53, 54], whose matrix elements satisfy $C_{m,n} = \frac{1}{2} [\rho \gamma_m \gamma_n] = \frac{1}{2} \langle \gamma_m \gamma_n \rangle$. The entanglement entropy is then

$$S_A = -\frac{1}{2} \sum_n [(1 - \lambda_n) \ln(1 - \lambda_n) + \lambda_n \ln \lambda_n], \quad (E2)$$

with λ_n the eigenvalues of $C_{m,n}$.

To measure the correlation matrix $C_{m,n}$ on a quantum

computer, we note that:

$$\begin{cases} C_{2m-1,2n-1} = \langle f_m^\dagger f_n^\dagger \rangle + \langle f_m f_n \rangle + \langle f_m f_n^\dagger \rangle + \langle f_m^\dagger f_n \rangle, \\ C_{2m,2n} = -\langle f_m^\dagger f_n^\dagger \rangle - \langle f_m f_n \rangle + \langle f_m f_n^\dagger \rangle + \langle f_m^\dagger f_n \rangle, \\ C_{2m-1,2n} = i\langle f_m^\dagger f_n^\dagger \rangle - i\langle f_m f_n \rangle + i\langle f_m f_n^\dagger \rangle - i\langle f_m^\dagger f_n \rangle, \\ C_{2m,2n-1} = i\langle f_m^\dagger f_n^\dagger \rangle - i\langle f_m f_n \rangle - i\langle f_m f_n^\dagger \rangle + i\langle f_m^\dagger f_n \rangle. \end{cases} \quad (E3)$$

This suggests that we need to measure four expectation values: $\langle f_m^\dagger f_n^\dagger \rangle$, $\langle f_m f_n \rangle$, $\langle f_m f_n^\dagger \rangle$ and $\langle f_m^\dagger f_n \rangle$. From the Jordan-Wigner transformation, we have:

$$\begin{cases} f_n = \sum_{j=1}^{n-1} \sigma_j^z \sigma_n^+, \\ f_n^\dagger = \sum_{j=1}^{n-1} \sigma_j^z \sigma_n^-, \end{cases} \quad (E4)$$

where $\sigma_n^+ = \frac{1}{2}(\sigma_n^x + i\sigma_n^y)$ and $\sigma_n^- = \frac{1}{2}(\sigma_n^x - i\sigma_n^y)$. Then the four different expectation values become

$$\begin{cases} \langle f_m^\dagger f_n^\dagger \rangle = \frac{1}{4} (C_{m,n}^{xx} - C_{m,n}^{yy} - iC_{m,n}^{xy} - iC_{n,m}^{yx}), \\ \langle f_m f_n \rangle = \frac{1}{4} (C_{m,n}^{xx} - C_{m,n}^{yy} + iC_{m,n}^{xy} + iC_{n,m}^{yx}), \\ \langle f_m^\dagger f_n \rangle = \frac{1}{4} (C_{m,n}^{xx} + C_{m,n}^{yy} + iC_{m,n}^{xy} - iC_{n,m}^{yx}), \\ \langle f_m f_n^\dagger \rangle = \frac{1}{4} (C_{m,n}^{xx} + C_{m,n}^{yy} - iC_{m,n}^{xy} + iC_{n,m}^{yx}), \end{cases} \quad (E5)$$

where:

$$C_{m,n}^{\alpha\beta} = \langle \sigma_m^\alpha \prod_{j=m}^{n-1} \sigma_j^z \sigma_n^\beta \rangle, \quad (E6)$$

with $\alpha, \beta = x, y$.

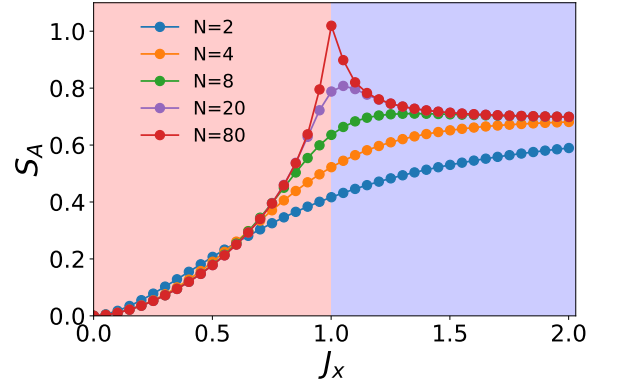


FIG. 7. The finite-size effect on the entanglement entropy of the 1D Kitaev spin chain: the signature of the quantum phase transition appears when the size of the lattice formed by bond fermions N is significantly larger than 10. The position of quantum phase transition point can be found accurately when $N \geq 80$. We define the subsystem A to be the equal partition of the lattice, and J_z is set to be 1.

Now we derive how to explicitly calculate the entanglement entropy of bond fermions of the 1D Kitaev spin chain, using the circuits in the main text. We begin the discussion with Eq. (B9), which can be rewritten as

$$\tilde{H}_{1D} = \sum_k \Psi_k^\dagger E_k \begin{pmatrix} \cos \theta_k & i \sin \theta_k \\ -i \sin \theta_k & -\cos \theta_k \end{pmatrix} \Psi_k, \quad (E7)$$

where Ψ_k is defined as Eq. (B8), and:

$$\begin{cases} E_k = \sqrt{(J_z D + J_x \cos k)^2 + J_x^2 \sin^2 k}, \\ \cos \theta_k = (J_z D + J_x \cos k)/E_k, \\ \sin \theta_k = J_x \sin k/E_k. \end{cases} \quad (\text{E8})$$

The Bogoliubov transformation is

$$\begin{pmatrix} b_k \\ b_{-k}^\dagger \end{pmatrix} = \begin{pmatrix} \cos \frac{\theta_k}{2} e^{-i\varphi_k/2} & \sin \frac{\theta_k}{2} e^{i\varphi_k/2} \\ \sin \frac{\theta_k}{2} e^{-i\varphi_k/2} & -\cos \frac{\theta_k}{2} e^{i\varphi_k/2} \end{pmatrix} \begin{pmatrix} \tilde{f}_k \\ \tilde{f}_{-k}^\dagger \end{pmatrix}, \quad (\text{E9})$$

where $e^{i\varphi_k} = i$, independent of k . This means that $\varphi_k = \pi/2$, independent of k . The correlations $\langle f_n f_m^\dagger \rangle$, $\langle f_n^\dagger f_m \rangle$, and $\langle f_n f_m \rangle$ are then determined from the ground state expectations of Bogoliubov fermions

$$\langle b_k b_{k'}^\dagger \rangle = \delta_{k,k'}, \quad \langle b_k^\dagger b_{k'} \rangle = \langle b_k^\dagger b_{k'}^\dagger \rangle = \langle b_k b_{k'} \rangle = 0. \quad (\text{E10})$$

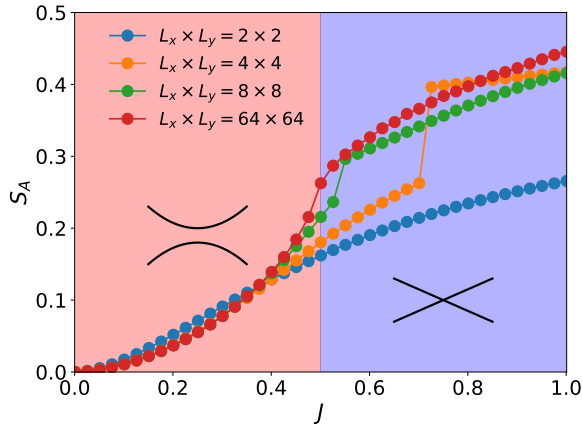


FIG. 8. The finite-size effects on the entanglement entropy of the Kitaev honeycomb model. The position of the quantum phase transition can be determined only when $L_x \times L_y \geq 64 \times 64$. Subsystem A is defined to be the equal partition of the lattice, and $J_z = 1$ and $J_x = J_y = J$.

Straightforward calculations show that:

$$\begin{aligned} \langle f_n^\dagger f_m^\dagger \rangle &= \frac{1}{N_k} \sum_k e^{-ik(n-m)} \frac{\sin \theta_k}{2} e^{-i(\varphi_k + \varphi_{-k})/2} \\ &= -i \frac{1}{N_k} \sum_k e^{-ik(n-m)} \frac{\sin \theta_k}{2}, \\ \langle f_n f_m \rangle &= \frac{1}{N_k} \sum_k e^{-ik(n-m)} \frac{\sin \theta_k}{2} e^{i(\varphi_k + \varphi_{-k})/2} \\ &= i \frac{1}{N_k} \sum_k e^{-ik(n-m)} \frac{\sin \theta_k}{2}, \\ \langle f_n f_m^\dagger \rangle &= \frac{1}{N_k} \sum_k e^{-ik(n-m)} \cos^2 \frac{\theta_k}{2}, \\ \langle f_n^\dagger f_m \rangle &= \frac{1}{N_k} \sum_k e^{-ik(n-m)} \sin^2 \frac{\theta_k}{2}, \end{aligned} \quad (\text{E11})$$

where N_k is the number of momentum points in the Brillouin zone. Note that $C_{2m-1,2n-1}$ and $C_{2m,2n}$ are the correlations of the real and imaginary parts of the fermions, respectively. As expected, we find $C_{2m-1,2n-1} = \delta_{m,n}$ and $C_{2m,2n} = \delta_{m,n}$. We also find that

$$C_{2m-1,2n} = i \sum_k e^{-ik(m-n)} (\cos \theta_k + \sin \theta_k) = i g_{m-n}, \quad (\text{E12})$$

and

$$C_{2m,2n-1} = -C_{2n-1,2m}. \quad (\text{E13})$$

The correlation between the two sites labeled by m and n is expressed by the following block matrix:

$$\begin{pmatrix} C_{2m-1,2n-1} & C_{2m-1,2n} \\ C_{2m,2n-1} & C_{2m,2n} \end{pmatrix} = \delta_{m,n} I_{2 \times 2} + i \Xi_{m-n}, \quad (\text{E14})$$

where:

$$\Xi_{m-n} = \begin{pmatrix} 0 & g_{m-n} \\ -g_{-(m-n)} & 0 \end{pmatrix}. \quad (\text{E15})$$

This means that for a subsystem containing N sites, the correlation matrix \mathcal{C} is given by

$$\mathcal{C} = I_{2N \times 2N} + i \begin{pmatrix} \Xi_0 & \Xi_1 & \cdots & \Xi_{N-1} \\ -\Xi_1^T & \Xi_0 & \cdots & \Xi_{N-2} \\ \vdots & \cdots & \ddots & \vdots \\ -\Xi_{N-1}^T & -\Xi_{N-2}^T & \cdots & \Xi_0 \end{pmatrix}. \quad (\text{E16})$$

We now focus on the two-site case. The correlation matrix becomes

$$\mathcal{C} = I_{2 \times 2} + i \Xi_0. \quad (\text{E17})$$

Particle-hole symmetry requires $\sin \theta_k = -\sin \theta_{-k}$. This implies that

$$g_0 = \frac{1}{N_k} \sum_{k \in \mathcal{K} \cup -\mathcal{K}} \cos \theta_k. \quad (\text{E18})$$

Using this expression, we obtain the exact curves in black shown in Fig. 3(c) and (d).

Another advantage of calculating entanglement entropy with correlation functions is that it allows us to study the finite-size effects on the entanglement entropy. In Fig. 7, we show how the entanglement entropy of the bond-fermions changes with increasing lattice size. We note that when the bond-fermion lattice size N is smaller than 10, the entanglement entropy increases with the coupling strength J_x monotonically, and no obvious signature appears when J_x passes through the quantum phase transition point. If we further increase the lattice size (for example the $N = 20$ case), the non-monotonic behavior of the entanglement entropy with increasing coupling strength starts to appear. However, an accurate determination of the quantum phase transition requires the bond-fermion lattice size N to be larger than 80.

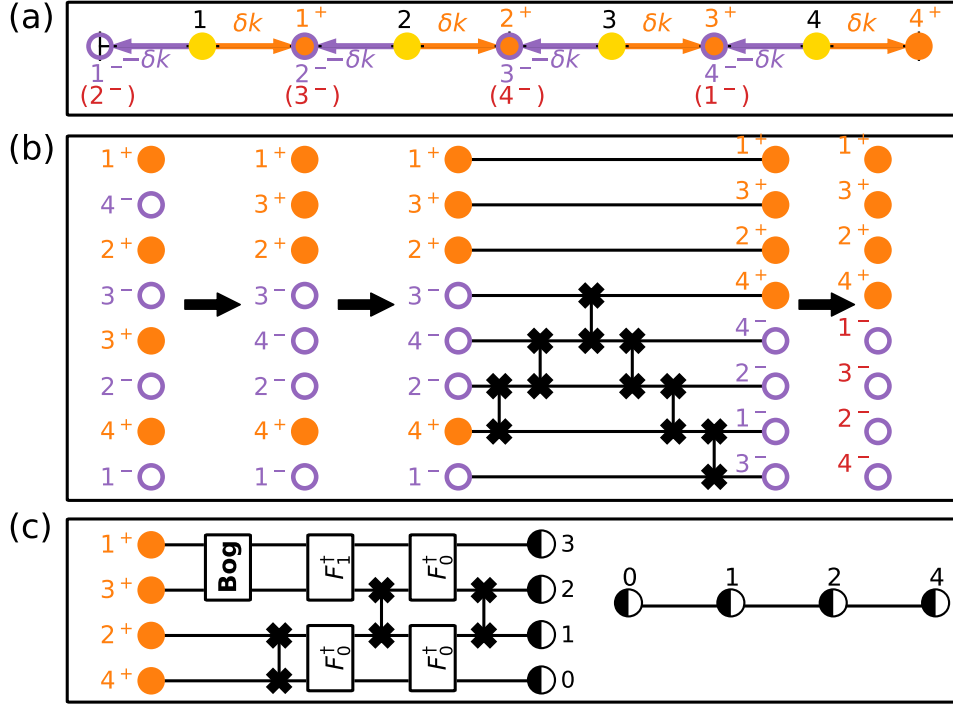


FIG. 9. Schematic illustration of the symmetry-enforced circuit using special momentum shifts: (a) momentum points before (the yellow dots) and after shifting (the orange and purple dots); (b) the simplification steps; (c) the quantum circuit transforming one of the copies from the momentum space to position space.

Similar procedures can be used to find the entanglement entropy of the bond fermions of the Kitaev honeycomb model. How the entanglement entropy changes with the increasing system size is shown in Fig. 8. It turns out that the accurate determination of the quantum phase transition requires a system size larger than $L_x \times L_y = 64 \times 64$.

Appendix F: Circuit simplification with special momentum shifts

Though in general, the symmetry-enforced circuit cannot be simplified, we show here that the circuit can be simplified for special momentum shifts. These special momentum shifts include the high symmetry points.

For a N -unit cell system, the discrete Fourier transformation and the particle-hole symmetry constraint requires the momentum points to be in the following set:

$$\mathcal{K} = \left\{ -\frac{N}{2} + \frac{1}{2}, -\frac{N}{2} + \frac{3}{2}, \dots, \frac{N}{2} - \frac{1}{2} \right\} \frac{2\pi}{N}, \quad (\text{F1})$$

where $N = 2^n$, with n a positive integer. As demonstrated in the main text, if we shift the momentum points by δk , their particle-hole partners must shift by $-\delta k$ to maintain particle-hole symmetry. Based on this, we note that $\delta k N / 2\pi = 1/2$ is a special point, which makes the

set of the momentum points by shifting δk to be identical to those that shift by $-\delta k$. Therefore, if the gap is *vanishing* at the high-symmetry points, the symmetry-enforced circuit can be decomposed into two identical copies.

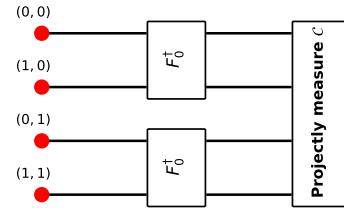


FIG. 10. Quantum circuit for measuring entanglement entropy of the Kitaev honeycomb model with the special momentum shift. The labels (k_x, k_y) in the unit of π denote the momentum points in the Brillouin zone.

The case with $N = 4$ case is shown in Fig. 9. The simplification requires three steps, which are shown in Fig. 9(b) from left to right. In the first step, we identify the momentum points labeled by 3⁺ and 4⁻, which is obvious from Fig. 9(a); in the second step, due to the gap vanishing at the high-symmetry points, the two-qubit Bogoliubov transformation becomes two separate single-qubit identity operations, so we can change the position of the momentum points 4⁺ and 3⁻ at the cost of a trivial

global phase; in the last step, we just renumber the $-\delta k$ -shifted momentum points by using the numbers in red shown below the original labels (in purple) in Fig. 9(a). Then one can easily find that the result yields two identical copies. We emphasize that the *vanishing* gap at the

high-symmetry points is essential in making this simplification possible.

It turns out that the Kitaev spin model fulfills this requirement, so the simplified circuit can be used to determine the different phases of the model. The details of the simplified circuits are shown in Fig. 10.

-
- [1] M. Schlosshauer, Decoherence, the measurement problem, and interpretations of quantum mechanics. *Rev. Mod. Phys.* **76**, 1267 (2005).
 - [2] A. M. Steane, Error correcting codes in quantum theory. *Phys. Rev. Lett.* **5**, 614 (2009).
 - [3] E. Knill, R. Laflamme, and W. Zurek, Threshold accuracy for quantum computation. Preprint at <https://arxiv.org/abs/quant-ph/9610011> (1996).
 - [4] D. Aharonov, and M. Ben-Or, Fault-tolerant quantum computation with constant error. *Proceedings of the 29th Annual ACM Symposium on Theory of Computing*, 176 (ACM, New York, 1997).
 - [5] B. M. Terhal, Quantum error correction for quantum memories. *Rev. Mod. Phys.* **87**, 307 (2015).
 - [6] A. Aliferis, D. Gottesman, and, J. Preskill, Quantum accuracy threshold for concatenated distance-3 codes *Quantum Inf. Comput.* **6**, 97 (2005).
 - [7] D. Bacon, Operator quantum error-correcting subsystems for self-correcting quantum memories. *Phys. Rev. A* **73**, 012340 (2006).
 - [8] A. G. Fowler, M. Mariantoni, J. M. Martinis, and A. N. Cleland, Surface codes: towards practical large-scale quantum computation. *Phys. Rev. A* **86**, 032324 (2012).
 - [9] D. K. Tuckett, S. D. Bartlett, and S. T. Flammia, Ultra-high error threshold for surface codes with biased noise. *Phys. Rev. Lett.* **120**, 050505 (2018).
 - [10] R. Chao, and B. W. Reichardt, Quantum error correction with only two extra qubits. *Phys. Rev. Lett.* **121**, 050502 (2018).
 - [11] M. Li, D. Miller, M. Newman, Y. Wu, and K. R. Brown, *Phys. Rev. X* **9**, 021041 (2019).
 - [12] A. Kitaev, Fault-tolerant quantum computation by anyons. *Ann. Phys.* **303**, 2 (2003).
 - [13] C. Nayak, S. H. Simon, A. Stern, M. Freedman, and S. D. Sarma, Non-Abelian anyons and topological quantum computation. *Rev. Mod. Phys.* **80**, 1083 (2008).
 - [14] S. D. Sarma, M. Freedman, and C. Nayak, Majorana zero modes and topological quantum computation. *NPJ Quantum Information* **1**, 15001 (2015).
 - [15] A. Kitaev, Anyons in an exactly solved model and beyond. *Ann. Phys.* **321**, 2 (2006).
 - [16] H. Yao, and S. A. Kivelson, Exact chiral spin liquid with Non-Abelian anyons. *Phys. Rev. Lett.* **99**, 247203 (2007).
 - [17] S. Yang, D. L. Zhou, and C. P. Sun, Mosaic spin models with topological order. *Phys. Rev. B* **76**, 180404 (2007).
 - [18] X.-Y. Feng, G. M. Zhang, and T. Xiang, Topological characterization of quantum phase Transitions in a Spin-1/2 Model. *Phys. Rev. Lett.* **98**, 087204 (2007).
 - [19] D. H. Lee, G. M. Zhang, and T. Xiang, Edge solitons of topological insulators and fractionalized quasiparticles in Two Dimensions. *Phys. Rev. Lett.* **99**, 196805 (2007).
 - [20] T. Si, and Y. Yu, Exactly soluble spin-1/2 models on three-dimensional lattices and non-abelian statistics of closed string excitations. Preprint at <https://arxiv.org/abs/0709.1302> (2007).
 - [21] Y. Yu, & Z. Q. Wang, An exactly soluble model with tunable p-wave paired fermion ground states. *Europhys. Lett.* **84**, 57002 (2008).
 - [22] G. Baskaran, G. Santhosh, and R. Shankar, Exact quantum spin liquids with Fermi surfaces in spin-half models. Preprint at <https://arxiv.org/abs/0908.1614> (2009).
 - [23] S. Mandal, and N. Surendran, Exactly solvable Kitaev model in three dimensions. *Phys. Rev. B* **79**, 024426 (2009).
 - [24] S. Ryu, Three-dimensional topological phase on the diamond lattice. *Phys. Rev. B* **79**, 075124 (2009).
 - [25] H. Yao, S.-C. Zhang, and S. A. Kivelson, Algebraic spin liquid in an exactly solvable spin model. *Phys. Rev. Lett.* **102**, 217202 (2009).
 - [26] C. Wu, D. Arovas, and H. H. Hung, Γ -matrix generalization of the Kitaev model. *Phys. Rev. B* **79**, 134427 (2009).
 - [27] K. S. Tikhonov, and M. V. Feigelman, Quantum spin metal state on a decorated honeycomb lattice. *Phys. Rev. Lett.* **105**, 067207 (2010).
 - [28] G. W. Chern, Three-dimensional topological phases in a layered honeycomb spin-orbital model. *Phys. Rev. B* **81**, 125134 (2010).
 - [29] F. Wang, Realization of the exactly solvable Kitaev honeycomb lattice model in a spin-rotation-invariant system. *Phys. Rev. B* **81**, 184416 (2010).
 - [30] V. Lahtinen, and J. K. Pachos, Topological phase transitions driven by gauge fields in an exactly solvable model. *Phys. Rev. B* **81**, 245132 (2010).
 - [31] G. Kells, J. Kailasvuori, J. K. Slingerland, and J. Vala, Kaleidoscope of topological phases with multiple Majorana species. *New J. Phys.* **13**, 095014 (2011).
 - [32] H. Yao, and D. H. Lee, Fermionic magnons, Non-Abelian spinons, and the spin quantum hall effect from an exactly solvable spin-1/2 Kitaev model with $SU(2)$ symmetry. *Phys. Rev. Lett.* **107**, 087205 (2011).
 - [33] H. H. Lai, and O. I. Motrunich, Power-law behavior of bond energy correlators in a Kitaev-type model with a stable parton Fermi surface. *Phys. Rev. B* **83**, 155104 (2011).
 - [34] V. Chua, H. Yao, & G. A. Fiete, Exact chiral spin liquid with stable spin Fermi surface on the kagome lattice. *Phys. Rev. B* **83**, 180412 (2011).
 - [35] R. Nakai, S. Ryu, and A. Furusaki, Time-reversal symmetric Kitaev model and topological superconductor in two dimensions. *Phys. Rev. B* **85**, 155119 (2012).
 - [36] Z. Nussinov, and J. van den Brink, Compass and Kitaev models: theory and physical motivations. *Rev. Mod. Phys.* **87**, 1 (2015).
 - [37] M. Hermanns, K. O'Brien, and S. Trebst, Weyl spin liquids. *Phys. Rev. Lett.* **114**, 157202 (2015).

- [38] O'Brien, K. Hermanns, M. & Trebst, Classification of gapless Z_2 spin liquids in three-dimensional Kitaev models. *Phys. Rev. B* **93**, 085101 (2016).
- [39] Z. Chen, X. Li, and T. K. Ng, Exactly Solvable BCS-Hubbard Model in Arbitrary Dimensions. *Phys. Rev. Lett.* **120**, 046401 (2018).
- [40] J.-J. Miao, H.-K. Jin, F.-C. Zhang, and Y. Zhou, Exact solution to a class of generalized Kitaev spin-1/2 models in arbitrary dimensions. *Science China Physics, Mechanics and Astronomy* **63**, 247011 (2020).
- [41] J.-J. Miao, H.-K. Jin, F. Wang, F.-C. Zhang, and Y. Zhou, Pristine Mott insulator from an exactly solvable spin-1/2 Kitaev model *Phys. Rev. B* **99**, 155105 (2019).
- [42] A. Stern, and N. H. Lindner, Topological quantum computation—from basic concepts to first experiments *Science* **339**, 1179-1184 (2013).
- [43] H. Yao, and X.-L. Qi, Entanglement entropy and entanglement spectrum of the Kitaev model. *Phys. Rev. Lett.* **105**, 080501 (2010).
- [44] K. Meichanetzidis, M. Cirio, J. K. Pachos and V. Lahtinen, Anatomy of fermionic entanglement and criticality in Kitaev spin liquids. *Phys. Rev. B* **94**, 115158 (2016).
- [45] G. Aleksandrowicz, *et al.* Qiskit: An open-source framework for quantum computing. <https://doi.org/10.5281/ZENODO.2562111> (2019).
- [46] F. Verstraete, J. I. Cirac, and J. I. Latorre, Quantum circuits for strongly correlated quantum systems. *Phys. Rev. A* **79**, 032316 (2009).
- [47] A. Cervera-Lierta, Exact Ising model simulation on a quantum computer. *Quantum* **2**, 114 (2018).
- [48] D. A. Ivanov, Non-Abelian Statistics of Half-Quantum Vortices in p -Wave Superconductors. *Phys. Rev. Lett.* **86**, 268-271 (2001).
- [49] P. Scholl, and R. Orus, Kitaev honeycomb tensor networks: Exact unitary circuits and applications. *Phys. Rev. B* **95**, 045112 (2017).
- [50] G. Vidal, and C. M. Dawson, Universal quantum circuit for two-qubit transformations with three controlled-NOT gates. *Phys. Rev. A* **69**, 010301 (2004).
- [51] J. A. Smolin, J. M. Gambetta, and G. Smith, Efficient method for computing the maximum-likelihood quantum state from measurements with additive gaussian noise. *Phys. Rev. Lett.* **108**, 070502 (2012).
- [52] A. J. Ferris, Fourier transform for fermionic systems and the spectral tensor network. *Phys. Rev. Lett.* **113**, 010401 (2014).
- [53] I. Peschel, Calculation of reduced density matrices from correlation functions. *J. Phys. A: Math.Gen.* **36**, L205-L208 (2003).
- [54] G. Vidal, J. I. Latorre, E. Rico, and A. Kitaev, Entanglement in Quantum Critical Phenomena. *Phys. Rev. Lett.* **90**, 227902 (2003).
- [55] H. Jiang, C.-Y. Wang, B. Huang, and Y.-M. Lu, Field induced quantum spin liquid with spinon Fermi surfaces in the Kitaev model. Preprint at <https://arxiv.org/abs/1809.08247> (2018).